


Magma chamber decompression during explosive caldera-forming eruption of Aira caldera

Nobuo Geshi ¹, Tadashi Yamasaki ¹, Isoji Miyagi¹ & Chris E. Conway¹

Decompression of a magma chamber is a fundamental condition of caldera collapse. Although theoretical models have predicted the decompression of magma chambers before caldera collapse, few previous studies have demonstrated the amount of magma chamber decompression. Here, we determine water content in quartz glass embayments and inclusions from pyroclastic deposits of a caldera-forming eruption at Aira volcano approximately 30,000 years ago and apply this data to calculate decompression inside the magma chamber. We identify a pressure drop from 140–260 MPa to 20–90 MPa during the extraction of around 50 km³ of magma prior to the caldera collapse. The magma extraction may have caused down-sag subsidence at the caldera center before the onset of catastrophic caldera collapse. We propose that this deformation resulted in the fracturing and collapse of the roof rock into the magma chamber, leading to the eruption of massive ignimbrite.

¹Research Institute of Earthquake and Volcano Geology, Geological Survey of Japan, AIST, Tsukuba, Japan. email: geshi-nob@aist.go.jp

Large-scale explosive eruptions that eject more than 100 km³ of magma are one of the most severe natural disasters on Earth, which have devastating impacts on human activities, both at regional and global scales^{1–6}. Such eruptions have various styles reflecting their tectonic environment, magma-system structures, and eruption-evolution processes⁷. Among them, one of the typical sequences involves a preceding Plinian eruption phase and/or an eruption of minor ignimbrite from a subsidiary vent, followed by caldera collapse and a catastrophic pyroclastic eruption from a ring-vent system^{7–12}. However, such “initial” activities do not always lead to a catastrophic caldera-forming eruption, as most Plinian eruptions cease without caldera collapse^{13,14}. Therefore, understanding the triggering mechanisms of caldera collapse is essential for predicting the evolution of such catastrophic explosive eruptions and for appropriate-disaster management responses⁶. Several theoretical approaches predict the decompression in a magma chamber required for the activation of caldera faults to induce caldera collapse^{7,15,16}. Few previous studies, however, have documented the amount of the decompression of the magma chambers in natural caldera-forming eruptions based on petrological investigations of the erupted magmas¹⁷. The degree of decompression for the activation of caldera faults may be variable among different calderas, as the activity of caldera faults is controlled by the degree of fault-system development and the tectonic stress environment in the host rock^{7,15,16}. Therefore, it is necessary to verify the decompression process of the magma chamber for each caldera-forming eruption using petrological evidence and to accumulate knowledge on the decompression conditions that induce caldera collapse.

Here, based on the variation in water content within volcanic glasses trapped in phenocrysts, we show that decompression of the magma chamber preceded caldera collapse, which resulted in a VEI 7 eruption at Aira volcano¹⁸ in southern Kyushu Island, Japan. Microanalytical measurements of the water content of volcanic glasses in the products of a geologically young caldera-forming eruption reveal the decompression process of the magma chamber that preceded caldera collapse. We traced the decompression of the magma chamber using the change in the water content in glass embayments within phenocrysts^{19–23} throughout the eruption sequence from the precursory stage to the main ignimbrite-forming eruption. Using the estimated decompression in the magma chamber, we also modeled the expected ground deformation in and around Aira volcano during the initial Plinian eruption phase.

Caldera-forming eruption of Aira volcano

The caldera-forming eruption of Aira volcano at around ~30,000 years ago (named the AT eruption) ejected approximately 400-km³ dense-rock equivalent (DRE) of high-silica rhyolite magma, which makes it one of the largest late-Pleistocene eruptions in the northwestern rim of the Pacific^{18,24}.

Aira caldera is one of the collapse calderas within the north–south trending Kagoshima graben in the southern part of Kyushu Island^{18,24,25} (Fig. 1a). Though several minor ignimbrites older than the Ito pyroclastic flow (mainly erupted in the middle Pleistocene) are distributed around the Aira caldera, there is no clear evidence for the existence of a collapse caldera at the present location of the Aira caldera before the AT eruption²⁴.

Similar to many caldera-forming eruptions, the sequence of the AT eruption had an initial stage with a Plinian phase and a minor phreatomagmatic pyroclastic flow that preceded the subsequent massive ignimbrite-forming phase with caldera collapse^{18,24}. Approximately 50 km³ of magma erupted during the initial stage to produce the Osumi pumice fall deposit (~40-km³ DRE^{26,27})

from the southern caldera rim²⁶, and subsequent Tsumaya pyroclastic flow deposit (~10-km³ DRE²⁸) erupted from the northern part of the caldera²⁴. The remaining 350 km³ of magma erupted to form a massive ignimbrite (Ito ignimbrite and its co-ignimbrite ash fall deposit named Aira-Tn ash fall deposit)^{18,24} after the onset of the caldera collapse, which is marked by the massive lag breccia at the base of the ignimbrite^{18,24,29} (Fig. 1).

Lack of evidence of a clear time gap, such as erosional surfaces or a pronounced oxidation zone in these deposits^{18,24,29}, suggests that all units of the AT eruption were emplaced continuously within a short period. Duration of the Plinian phase of the Osumi pumice fall deposit at the beginning of the AT eruption is estimated as ~2.8 days based on the total mass of the pumice fall deposit^{26,27} (~40 km³, corresponding to $\sim 1 \times 10^{14}$ kg) and the magma-discharge rate³⁰ ($\sim 4.2 \times 10^8$ kg s⁻¹) estimated from the distribution of the deposit. No clear flow and cooling unit were identified within the Ito ignimbrite, which implies a short duration for the eruption and emplacement of the ignimbrite^{18,24,29}. The analysis of the seasonal variation of the pollen fossils found in the products of the AT eruption also suggests that the AT eruption lasted 1–2 months³¹.

Most of the products of the AT eruption have a high-silica rhyolite composition with whole-rock SiO₂ content between 74 and 77 wt%^{32,33}. The phase-equilibrium relationship of the phenocrysts and the volatile concentrations in the glass inclusions in the phenocrysts suggest that the rhyolite magmas were stored at 140–260 MPa, corresponding to ~5–10 km below sea level assuming the density of the host rock as 2700 kg m⁻³^{32,33}.

Results

We measured the water contents in glass embayments and glass inclusions in the phenocrysts of the ejecta throughout the AT-eruption sequence. A glass embayment is a glass-filled channel found inside a phenocryst, one side of which is open to the surface of the phenocryst and connected to the external groundmass glass, and the other side is closed inside the phenocryst. The glass embayments are filled by silicate glasses with rhyolite composition (~78 wt% of SiO₂) (Supplementary Data 1 and 2).

We measured the distribution of water content inside the glass embayments as a function of the distance from the embayment entrance to reveal the profile of water content along the glass embayments (Fig. 2a). In cases where the water content at the deeper part of the embayment is greater than 5 wt%, the water content inside the embayment is relatively constant and decreases toward the entrance of the embayment within 50–100 micrometers from the entrance. In cases where the water content at the deeper part of the embayment is less than 5 wt%, the water content inside the embayment is almost constant. The relatively flat profile of the water content at the deeper part of the glass embayment is named “plateau”.

The water content in the plateau parts shows the systematic decrease along the stratigraphy of the deposits from 5–7 wt% to approximately 4–6 wt%, from the basal part of the Osumi pumice fall deposit to the top of the Osumi pumice fall deposit (Fig. 2b). The range of water content in the plateau parts is almost constant from the basal to the middle parts of the Osumi pumice fall deposit. The decrease of water content in the plateau parts becomes clear from the middle to upper parts of the Osumi pumice fall deposit (Fig. 2a and b). The water contents in the plateau parts ranging from 2 to 4 wt% were obtained from the Tsumaya pyroclastic flow deposit erupted just before the caldera collapse (Fig. 2b). Assuming that the partial pressure of water in the magma was equal to the total magmatic pressure, as the concentrations of CO₂ and other volatile phase are negligible (less than 250 ppm³³), the water

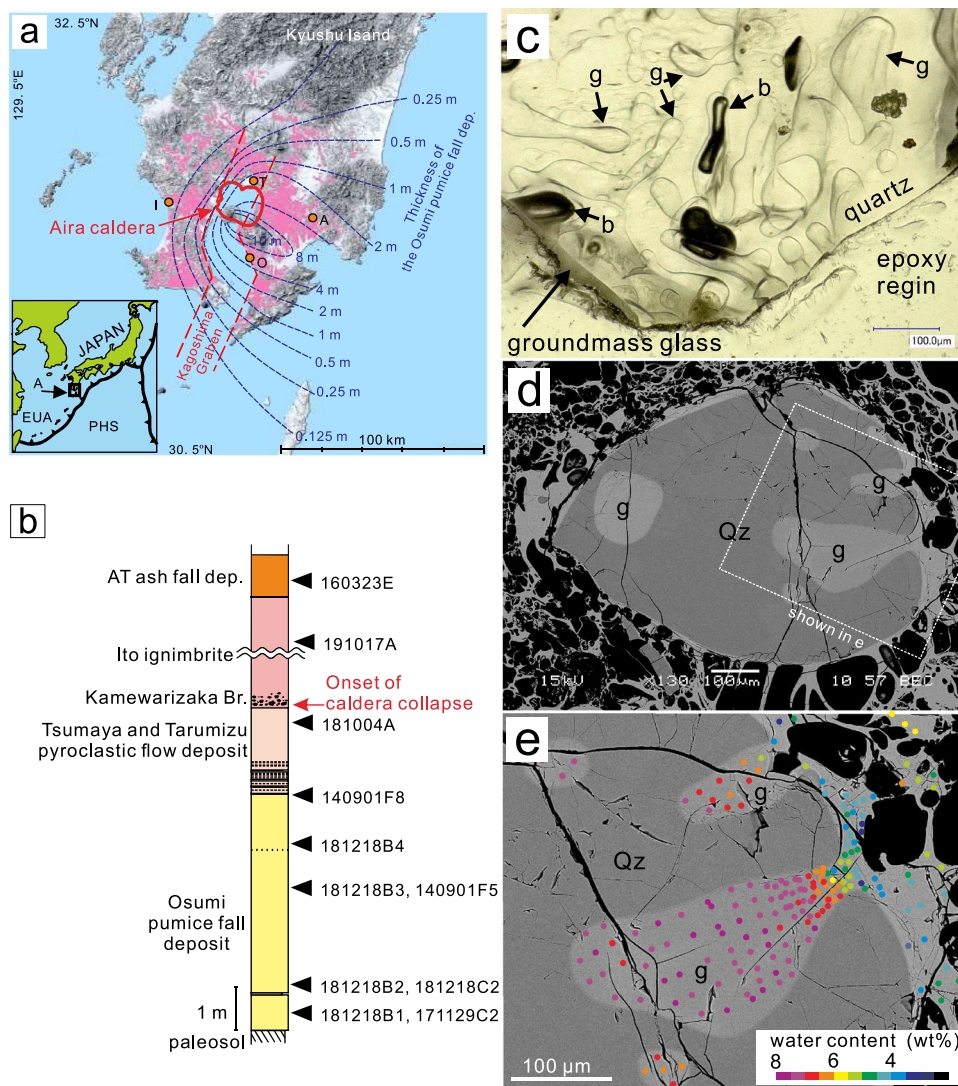


Fig. 1 Overview of AT-eruption products. **a** Distribution of products of the AT eruption. Inset shows the location of the Aira caldera. The solid red line indicates the topographic rim of the Aira caldera, broken blue lines are the isopach lines that represent the thickness of the Osumi pumice fall deposit, and the pink-colored area represents the distribution area of Ito ignimbrite. Orange circles with labels “O”, “T”, “I”, and “A” show the sampling locations of the Osumi pumice deposit, Tsumaya pyroclastic flow deposit, Ito ignimbrite, and the AT ash fall deposit, respectively. **b** Schematic stratigraphy of the eruptive products of the AT eruption showing sampling depths. **c** Optical microscopic image of glass embayments in a quartz phenocryst of the Osumi pumice fall deposit (sample id: 140901F8). This microphotograph was taken through a polished surface of a quartz phenocryst embedded in epoxy resin, showing the glass embayments on the crystal surface of the quartz. Labels “g” indicate representative glass embayments. Labels “b” show the bubbles in glass embayments. **d** Backscattered electron image of a quartz phenocryst (Qz) with several glass embayments (g) found in a quartz phenocryst from the Osumi pumice fall deposit (sample id: 171129C2). **e** Distribution of water content in the glass embayment and surrounding groundmass glasses. The colored circles indicate the analysis point and the color of each circle represents the quantified water content at each analysis point.

content in the glass can be converted to the pressure based on water solubility in the rhyolite melt³⁴. The water contents obtained from the basal–middle part of the Osumi pumice fall deposit (5–7 wt%) correspond to the solubility of the water at 140–260 MPa. The water contents obtained from the uppermost part of the Osumi pumice fall deposit (4–6 wt%) and the Tsumaya pyroclastic flow deposit (2–4 wt%) correspond to the solubility of the water at 90–190 MPa and 20–90 MPa, respectively. The water content in the plateau parts of the embayments hosted in the Ito ignimbrite and its cognimbrite ash ranges from 1.5 to 3.5 wt%, which corresponds to pressure conditions of 15–70 MPa (Fig. 2b).

In contrast to the clear decrease of the water content in glass embayments toward the eruption of the main ignimbrite, isolated glass inclusions have a similar range of water contents (5–7 wt%) without any clear trends throughout the stratigraphy (Fig. 2c).

The range of water contents in the isolated glass inclusions was similar to that of glass embayments of the pumice collected from the basal part of the Osumi pumice fall. The water contents of 5–7 wt% in the isolated glass inclusions found in the Osumi pumice fall and the Tsumaya pyroclastic flow deposits correspond to a pressure of approximately 140–260 MPa, which is equivalent to depths of 5.3–9.8 km assuming the density of the host rock as 2700 kg/m³. This estimate is consistent with the pressure in the magma chamber based on the phenocryst-phase equilibrium relationships stated in previous studies^{32,33}.

Two-step decompression of magmas. The profile of water content with two regions of different gradients, which is typically observed in the glass embayments (Fig. 2a), indicates that the

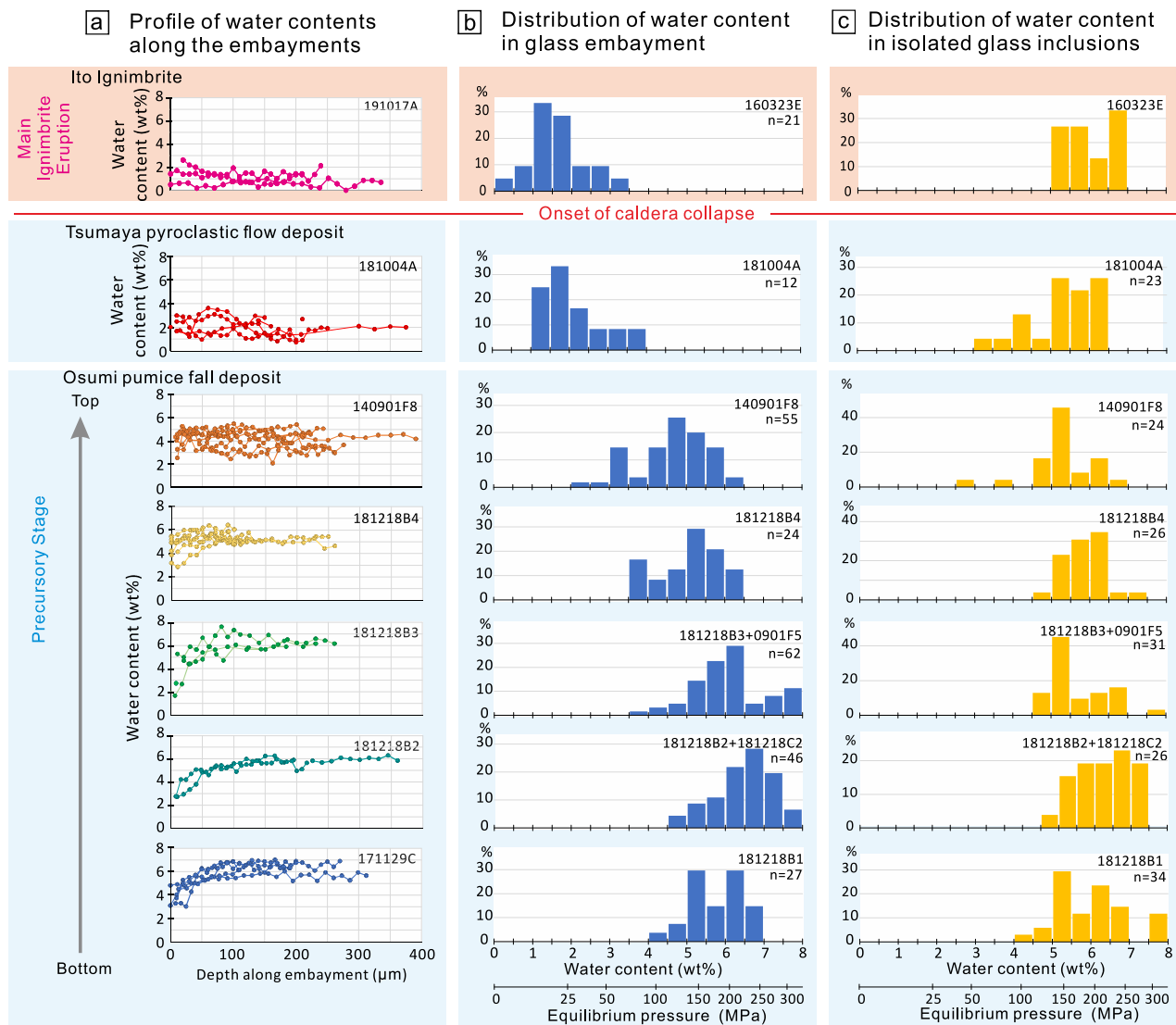


Fig. 2 Variations in water content in glass embayments and inclusions. **a** Line profile of water content along the glass embayments. The distance shown in the horizontal axis of each diagram corresponds to the depth of the measured point from the entrance to the glass embayment. **b** Variation in water content of the plateau part of the glass embayment found in the quartz phenocrysts (deeper than $\sim 100 \mu\text{m}$ from the surface of the phenocryst). Vertical axis shows the percentage. **c** Variation in water content of the isolated glass inclusions in the orthopyroxene and quartz phenocrysts. Vertical axis shows the percentage.

magma has experienced two stages of decompressional dehydration with different decompression rates (Fig. 3).

With the dehydration of the melt outside of an embayment, the water content inside the embayment decreases by the diffusion of water through the entrance of the embayment. The diffusion will form a gradient of water content along the embayment. The steepness of the gradient depends on the dehydration rate of the surrounding melt and the length of the embayment. The existence of a plateau of water content in the embayments, as found in the ejecta of the AT eruption, indicates that the distribution of water inside and outside the embayment has been homogenized by diffusion with the slow dehydration rate in the surrounding melt. Assuming that the water content in the plateau records the saturated water content in the decompressing magma chamber when the magma was tapped from the chamber, the change of the water content in the plateau along the stratigraphic sequence of the eruption (Fig. 2b) can be regarded as a record of the decompression process of the magma chamber.

The decrease of water contents in the plateau parts along the stratigraphy of the deposits shows that the magma chamber was

depressurized from 140–260 MPa, which is the original magmatic pressure, to 90–190 MPa by the end of the eruption of the Osumi pumice fall deposit ($\sim 40 \text{ km}^3$), and further depressurized to 20–90 MPa by the subsequent eruption of the Tsumaya pyroclastic flow ($\sim 10 \text{ km}^3$). The caldera collapse occurred when the magmatic pressure in the magma chamber dropped to 20–90 MPa, due to the extraction of $\sim 50 \text{ km}^3$ of magma that produced the Osumi pumice fall and the Tsumaya pyroclastic flow. Our one-dimensional diffusion model shows that the decompression rate less than $1 \times 10^3 \text{ Pa s}^{-1}$ was necessary to decrease the water contents in the plateau from 6.5% to 4.0% keeping the variation of water contents less than 0.5 wt% in the plateau part (Fig. 3a and Supplementary Data 1). The decrease of the water content from 6.5 to 4% seen in the plateau parts during the eruption of the Osumi pumice fall is considered to have taken about 48 h or more at this decompression rate (Fig. 3a). This result is consistent with the estimated decompression rate ($2.2\text{--}7.0 \times 10^2 \text{ Pa s}^{-1}$) from the duration of the Plinian phase of the Osumi pumice fall deposit (~ 2.8 days) estimated from the magma-discharge rate and total volume of erupted magma. This

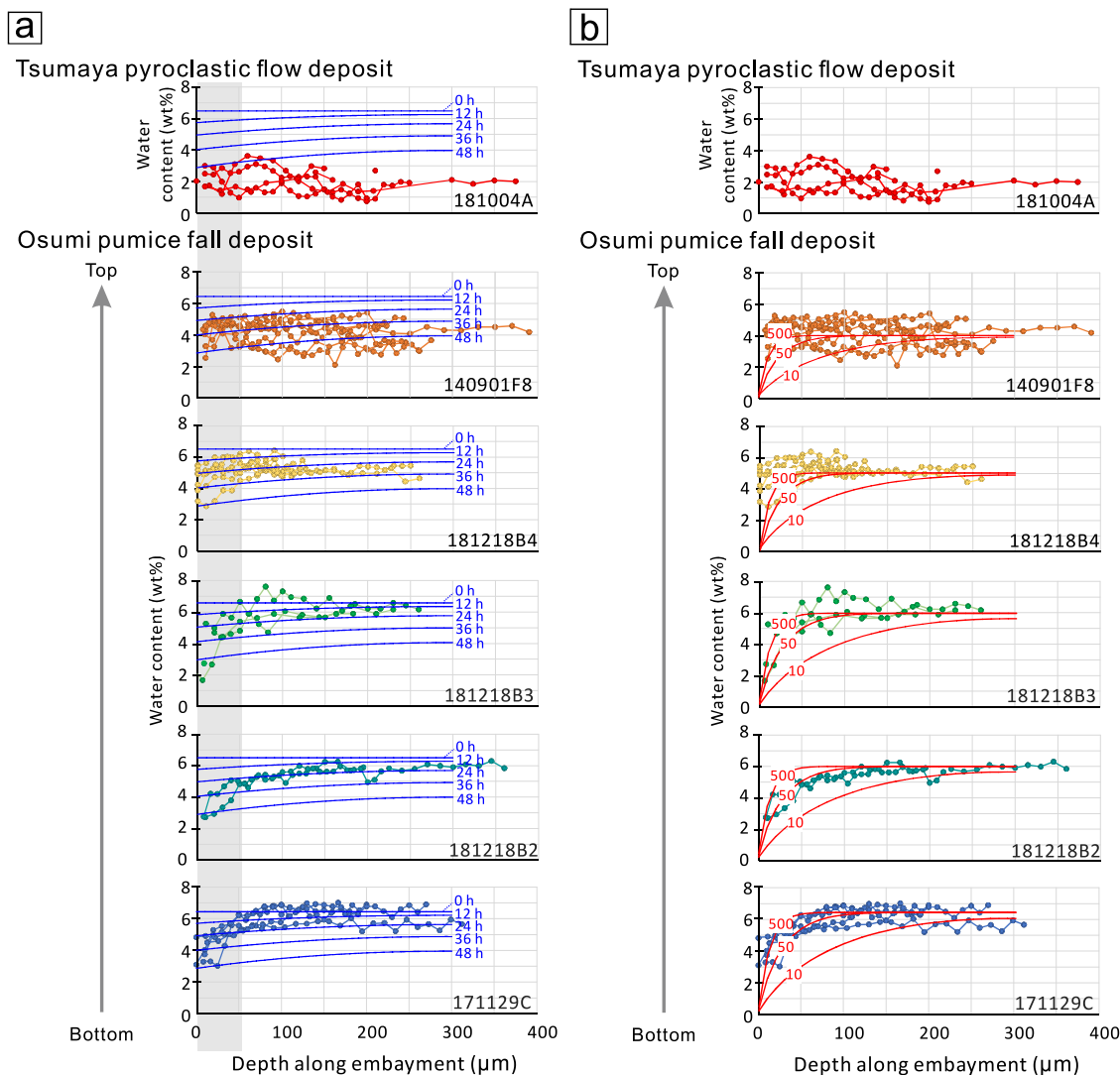


Fig. 3 Two-step dehydration. **a** Distributions of water content along a 300- μm -long melt embayment calculated by the one-dimensional diffusion model. The decompression rate is assumed as $1 \times 10^3 \text{ Pa s}^{-1}$. The initial water content is 6.5 wt%. The distributions of water 12, 24, 36, and 48 h after the start of decompression are shown. The measured data of water contents shown in each panel are the same as those in Fig. 2a. The gray hatched area ($\sim 50 \mu\text{m}$ from the entrance of the embayment) is considered to be affected by the rapid dehydration in the second decompression step and/or post-eruption hydration. **b** Diffusion profiles formed in the embayment when the magma is decompressed to atmospheric pressure at different decompression rates, calculated by the one-dimensional diffusion model (red solid line). The numbers shown in the profiles indicate the decompression rate ($\times 10^3 \text{ Pa s}^{-1}$). The initial water content of sample 171129 C is 6.5 wt%, samples 181218B2 and 181218B3 are 6.0 wt%, 181218B4 is 5.0 wt%, and 140901F8 is 4.0%, decreasing with the progress of the eruption.

decompression rate of the magma chamber is also consistent with the estimation ($< 10^3 \text{ Pa s}^{-1}$) from the number density of “phenobubbles” in the Osumi pumice, which were formed in the magma chamber³⁵.

The steep gradient of water content at the entrance of the embayments (Fig. 2a) records a much higher decompression rate, which occurred after the formation of the plateau. The one-dimensional diffusion models indicate that the decompressional dehydration between 50 and $500 \times 10^3 \text{ Pa s}^{-1}$ can form the observed profile of water content in the glass embayments of the Osumi pumice fall (Fig. 3b). The estimated decompression rate from glass embayments is more than three orders of magnitude lower than those based on vesicle-number density of the matrix bubbles ($\sim 10^8 \text{ Pa s}^{-1}$)³⁵. As pointed out in the similar example of the Santorini volcano²³, the difference between two estimated decompression rates suggests the acceleration of decompression rate of magmas during the ascent in the conduit from

$< 5 \times 10^4 \text{ Pa s}^{-1}$ in the deeper portion of the conduit recorded in the diffusion profile of the glass embayments to $\sim 10^8 \text{ Pa s}^{-1}$ in the shallower portion of the conduit recorded by the matrix bubbles. However, the actual decompression rates of magmas may have a deviation from this estimation assuming a one-dimensional diffusion in a straight and cylindrical embayment due to the complex shapes of actual embayments (Fig. 1c and d), such as necking and curvature³⁶. The absence of clear gradients of water content at the entrance of the embayments in the ejecta of the later stage of the eruption (Fig. 2a) is a result of the smaller contrast of water content in the diffusion profile due to the decrease of the water content in the plateau part. Hydration in the post-eruption period also overprints the diffusion profile with low contrast.

These results indicate that the first step of decompression, which is recorded in the plateau of water content, is the decompression process of the magma chamber due to the

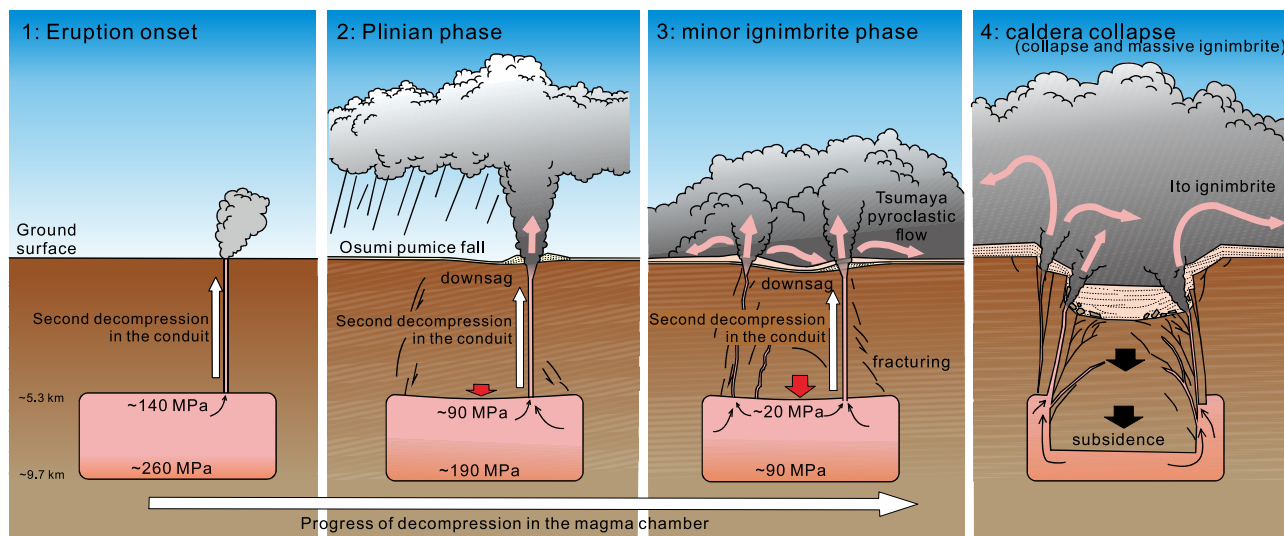


Fig. 4 Evolution of magma decompression during the AT eruption. Decompression of magma chamber and deformation of the host rock toward the caldera collapse and eruption of massive ignimbrite. A rhyolite magma chamber was subjected to lithostatic pressures of 140–260 MPa, corresponding to depths of 5.3–9.4 km below the surface of the Aira volcano before the eruption. Extraction of magmas from the magma chamber caused decompression in the magma chamber. Pressure in the magma chamber decreased to ~90–190 MPa due to the extraction of the magma by the eruption of the Osumi pumice fall during the Plinian phase. Down-sag deformation of the roof rock was initiated by the pressure difference between the lithostatic pressure acting on the host rock of the magma chamber and the decreasing magmatic pressure in the chamber during the Plinian phase. The extracted magmas were decompressed rapidly during their ascent through the conduit to the ground surface. Caldera collapse started when blocks of roof rock detached by the ring fracture subsided into the magma chamber. The subsidence of the blocks into the magma chamber accelerated further magma output, to form a massive ignimbrite.

extraction of magmas toward the caldera collapse. The second step of decompression recorded in the diffusion profile at the entrance of the glass embayments is the rapid decompression during the ascent of magma through the conduit.

Decompression of the magma chamber and caldera collapse.

The estimated decompression of the magma chamber prior to caldera collapse inferred from the water content in the plateau is consistent with the results from theoretical models¹⁶. Caldera collapse occurs when decompression of the magma chamber by rapid extraction of magma exceeds the threshold of fracturing and faulting in the roof rock of the chamber (Fig. 4). The amount of decompression that is required for a cylindrical caldera block to descend into an underlying magma chamber can be expressed as a function of the depth to the magma chamber and the diameter of the caldera fault¹⁶. In the case of the Aira caldera, the depth to the magma chamber was estimated to be approximately 6 km, based on the constraints from the water content in glass inclusions, and the horizontal diameter of the caldera fault was estimated to be approximately 14 km, assuming that the size of the topographic caldera floor indicates that of the top of the caldera block. According to the model proposed by a previous study¹⁶, if the magmatic pressure at the top of the magma chamber drops ~120 MPa from the lithostatic pressure, faults will be activated for a caldera with a size similar to that of Aira volcano. A large-scale decompression of the magma chamber, which exceeded half of the lithostatic pressure at the roof of the magma chamber, before the onset of caldera collapse, indicates that Aira caldera is a typical example of an “under-pressure caldera”⁷ that requires a large underpressure in the magma chamber for formation and activation of caldera faults. The absence of a previous caldera structure before the AT eruption suggests that the fault system of the Aira caldera needed to be fully generated during the AT eruption. The high shear strength of the host rock due to the absence of the previous caldera structure allowed a large decompression in the magma reservoir before the caldera started to collapse.

Though the decompression estimated from the glass embayments is slightly larger than the theoretical prediction, the decompression in the magma chamber, leading to the activation of caldera faults, should be greater than the modeled value obtained using a simple piston-cylinder fault, considering the complex structure of a caldera fault with branching^{37,38} and down-sag deflection of the host rock^{39,40}.

The <0.5 wt% to 3.5 wt% range of water contents in the embayments of Ito ignimbrite and its co-ignimbrite ash erupted with the caldera collapse (Fig. 2b) suggests the extraction of magmas from various depths of the magma chamber with different pressure conditions. Decompression of a magma stored in the shallow part of the magma chamber during the precursory stage induced the collapse of the roof of the magma chamber, and enhanced the extraction of the magmas stored in the melt bodies distributed in the different parts of the crystal mush body⁴¹.

Ground deformation prior to the caldera collapse. Progressive magma extraction from the magma chamber during the precursory stage may cause down-sag deformation^{39,40} and fracturing of the roof rock of the magma chamber^{37,38}. Based on the estimated volume of magma extracted from the magma chamber of the AT eruption, the expected ground deformation has been modeled by an elastic deformation model, assuming a cylindrical magma chamber with a horizontal diameter of 14 km and a vertical length of 3 km at a depth of 6 km from the ground surface at the center of the Aira caldera (Fig. 5a). The volume of this magma chamber corresponds to the total volume of the erupted magma during the AT eruption^{18,24}. The model shows that the subsidence of the ground surface just above the center of the magma chamber was estimated to be >150 m (Fig. 5b and c) when 40 km³ of magma, equivalent to the total volume of the erupted magma that produced the Osumi pumice fall deposit, was extracted from this magma chamber. The area where subsidence exceeded 10 m is expected to be within a 13-km radius from the center of the magma chamber. Assuming that the magma chamber is located at the center of Aira caldera, ~50 m of

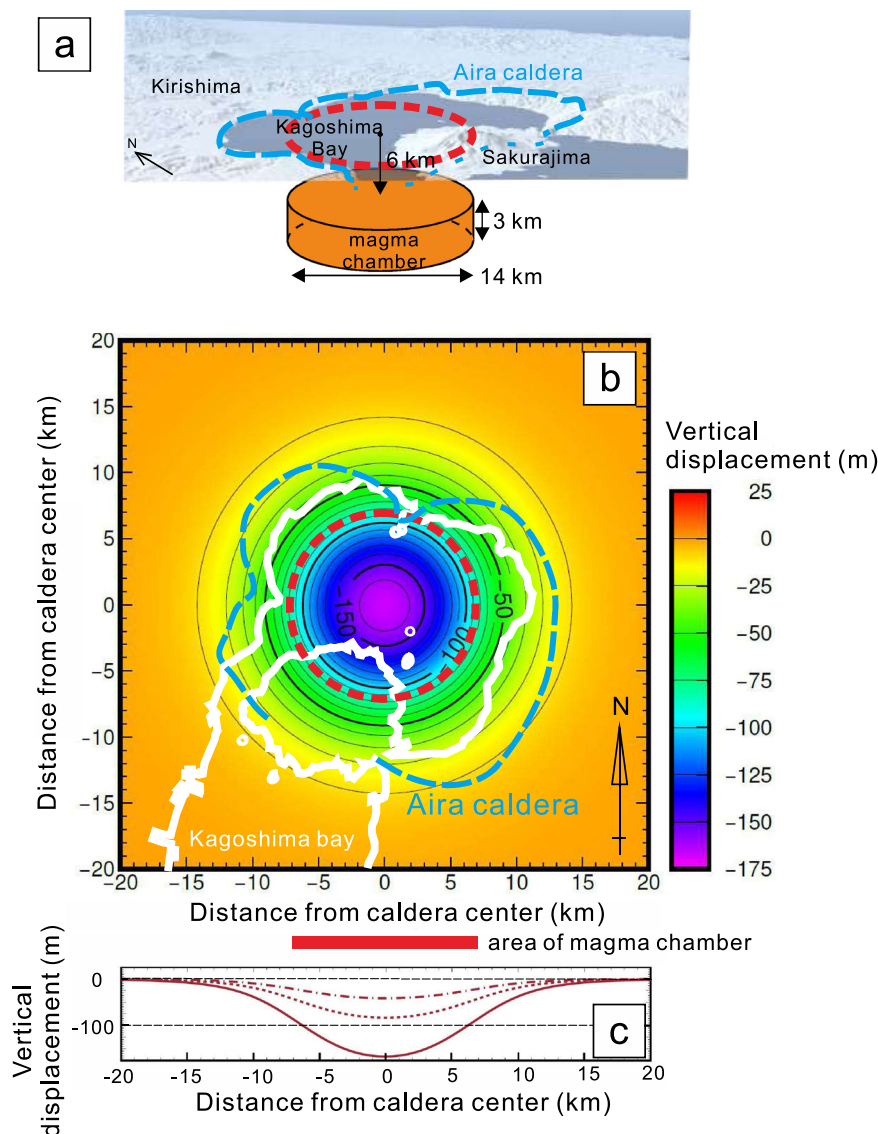


Fig. 5 Configuration and results of modeling deformation during caldera collapse. **a** Outline of the configuration of the model. A cylindrical magma chamber with a horizontal diameter of 14 km and a vertical length of 3 km at the depth of 7 km from the ground surface is assumed for the simulation. The magma chamber is centered on the center of the Aira caldera. Broken red line shows the projection of the magma chamber to the present sea level. Broken blue line is the current topographic caldera rim. **b** Calculated vertical displacement of ground surface at the end of the eruption of the Osumi pumice fall due to the 40-km³ extraction of magma from a magma chamber beneath the Aira caldera. The minus sign indicates subsidence. The contour interval is –10 m. Broken red line and blue line mark the projection of the magma chamber to the present sea level, and the topographic caldera rim, respectively. White solid line shows the current coastline. **c** The vertical displacement profile as a function of the distance from the deformation center after the extraction of magma from the chamber with a volume of (dashed and dotted) 10, (dotted) 20, and (solid) 40 km³. The inverted triangles mark the distance corresponding to the perimeter of the magma chamber.

subsidence is expected at the coastline of Kagoshima Bay due to the eruption that produced the Osumi pumice fall deposit (Fig. 5b and c). Judging from the estimated duration of the Osumi pumice fall eruption, this ground deformation occurred within ~3 days from the onset of the eruption. Such rapid and massive caldera subsidence may have caused seawater intrusion into the caldera area, resulting in violent phreatomagmatic explosions during the eruption of the Tsumaya pyroclastic flow at the end of the precursory stage.

Extensive deformation of the roof rock enhanced fracturing in the roof rock, and resulted in the propagation and enlargement of the conduits, as observed in the case of the eruptions of the Osumi pumice fall and Tsumaya pyroclastic flow^{18,24}. The propagation and enlargement of the conduits during the

eruptions of the Osumi pumice fall and Tsumaya pyroclastic flow maintained or increased the magma discharge flux toward the onset of caldera collapse, despite the progress of decompression in the magma chamber²⁷. The decompression of the magma chamber may have been accelerated by an increase in the magma flux due to the expansion of the conduit, resulting in the threshold for caldera collapse being exceeded.

Discussion

The results of this study reveal that the decompression of the magma chamber from 140–260 MPa to 20–90 MPa, due to the extraction of ~50 km³ of magma as the Osumi pumice fall deposit and the Tsumaya pyroclastic flow, triggered the collapse of the

Aira caldera and the eruption of $\sim 350 \text{ km}^3$ of magma that produced the Ito ignimbrite, which accounts for 88% of the total volume of the magma erupted during the AT eruption. Therefore, detection of the degree of magma-chamber decompression during a “precursory stage” is crucial for the prediction of the eruption of a catastrophic ignimbrite as the decompression of the magma chamber can cause caldera collapse.

The Plinian phase of the Osumi pumice fall is characterized by the extraction of a large volume of magma ($\sim 40 \text{ km}^3$ ^{3,26,27}) with a high eruption rate ($\sim 4.2 \times 10^8 \text{ kg s}^{-1}$ ³⁰), which is two orders higher than that of the largest historical eruption of Sakurajima, post-caldera volcano of the Aira caldera, in 1914 (0.09-km³ DRE⁴², $5 \times 10^6 \text{ kg s}^{-1}$ ⁴³). The 1914 eruption resulted in only $\sim 1 \text{ m}$ of subsidence at the caldera rim⁴⁴, with the extraction of a total of 1.5 km^3 of magma mainly as a lava flow from the Aira caldera. This comparison suggests that a future eruption that precedes caldera collapse is expected to cause much larger and faster ground deformation than what has been experienced during historic eruptions. This case study in the Aira caldera confirms that extensive decompression of a magma chamber, and the consequent deformation of the roof rock and the enlargement of the conduit^{12,16,27}, are thought to be the branching mechanism from a “normal” Plinian eruption to the eruption of a massive ignimbrite-forming pyroclastic flow associated with caldera collapse. Therefore, we conclude that monitoring the intensity of ground deformation during an eruption would allow the total decompression of a magma chamber to be estimated, and thereby prediction of the potential of caldera collapse and initiation of a massive ignimbrite-forming eruption.

Methods

Sampling. A series of AT-eruption products were collected for petrological investigation. The pumice clasts of the Osumi pumice fall deposit were collected from an outcrop along the eastern coast of Kagoshima Bay, $\sim 26 \text{ km}$ southeast of the caldera center (Shinjo Fumoto, Tatumizu City), where the thickness of the Osumi pumice fall deposit at the outcrop is approximately 5 m (Fig. 1). The Osumi pumice fall deposit in the outcrop consists of a nonwelded pile of lapilli-size clasts of rhyolite pumice. The size of clasts shows upward coarsening; maximum clast size varies from $\sim 4 \text{ cm}$ at the bottom to $\sim 12 \text{ cm}$ at the top of the deposit. The Osumi pumice fall deposit in this outcrop is covered by an $\sim 3\text{-m}$ -thick Tatumizu pyroclastic flow deposit⁴⁵. The pumice clasts were collected from six different levels of the deposit of the outcrop.

The pumice samples of the Tsumaya pyroclastic flow deposit were collected from an outcrop $\sim 11 \text{ km}$ northeast of the caldera center (Near Shiroyama Park, Kirishima City). The thickness of the Tsumaya pyroclastic flow deposit was approximately 8 m . The Tsumaya pyroclastic flow deposit at the outcrop consists of nonwelded stratified ash-flow deposit. The presence of accretionary lapilli in the deposit suggests the low-temperature emplacement of the deposit.

The pumice samples of the Ito ignimbrite, which is the main ejecta of the AT eruption, were collected from the western coast of Satsuma Peninsula, 35 km west of the caldera center (Fukiage Beach, Hioki City). The Ito ignimbrite at this site is a nonwelded pumice-rich flow deposit approximately 80-m -thick. The AT ash-fall deposit was collected from an outcrop $\sim 40 \text{ km}$ southeast of the caldera center (Shibushi City). In this outcrop, an $\sim 4\text{-m}$ -thick AT ash-fall deposit covers the Ito ignimbrite.

Sample collections are conducted not in areas that require permission for sample collection, such as nature parks or nature-conservation areas. Some samples were collected on private land with the permission of the landowners.

Measurements. To investigate the decompression process throughout the sequence of the caldera-forming eruption, we analyzed the water content of glass inclusions and embayments in phenocryst crystals. The high-silica rhyolite erupted during the AT eruption contained up to $\sim 23 \text{ vol.}\%$ of plagioclase, orthopyroxene, and quartz crystals as phenocrysts³². Minor volumes of magnetite and ilmenite were also found as phenocrysts. The quartz phenocrysts exhibited corroded outlines with embayments due to the heating of rhyolite magma by the mafic injection just prior to the AT eruption³².

The phenocryst crystals were extracted from crushed pumice samples. The separated phenocryst crystals were fixed in epoxy resin and then polished to expose the glass embayment and inclusions. The polished surfaces of the crystals were coated with carbon for analysis with a scanning electron microscope (SEM). The thickness of the carbon coating on the samples ranged from 35 to 45 nm .

It is difficult to distinguish whether the glass region exposed on the polished surface is a part of the embayment or a glass inclusion closed inside the crystal because embayments that extend obliquely to the polishing surface are, in most cases, only partially exposed to the polishing surface. To determine whether the glass region exposed on the polished surface is part of the embayment, we used transmitted light observation with an optical microscope, and determined that the glass embayment is continuous with the groundmass glass outside the crystal. The longitudinal section of the embayment was exposed to the observation surface by polishing while observing with an optical microscope to measure the compositional profile along the embayment. After confirming that glass inclusions were completely enclosed in the crystal by observation using an optical microscope, we proceeded with polishing to expose the glass inclusions on the polished surface to measure their chemical composition.

The chemical composition of the volcanic glass was determined using an energy-dispersive X-ray spectrometer (EDS), X-Max 20 of Oxford Instrumentals, mounted on the SEM JEOL JSM6610LV at the Geological Survey of Japan. The beam current for the measurement was 1.000 nA and the acceleration voltage was 15 kV . We analyzed an area larger than $\sim 10 \mu\text{m}^2$ for each analysis to avoid damage to the glass and loss of alkaline elements. The detection limit of these elements was less than approximately $0.1 \text{ wt}\%$.

The water content in glass was determined using the stoichiometric balance between the oxygen and cation elements in the analyzed area^{32,46,47}. Elements with larger atomic numbers than oxygen were quantified using EDS by the software INCA of Oxford Instrumentals. O, Na, Mg, Al, Si, P, K, Ca, Ti, Mn, and Fe were detected in the analyzed glasses. Assuming that all elements form oxides, the quantified oxygen was distributed according to the valence of each element. Assuming that the excess oxygen formed H_2O , the water content in the volcanic glass was calculated. All iron in the glass was in the form of ferric oxide (Fe^{3+}). Because the composition of glass embayments and inclusions in the samples were rhyolite with less than $1.1 \text{ wt}\%$ of iron, the error of quantification of H_2O caused by the estimation of $\text{Fe}^{2+}/\text{Fe}^{3+}$ ratio is less than $0.2 \text{ wt}\%$. Analytical results are shown in Supplementary Data 1 and 2.

The quantified value of the H_2O content in representative glass samples was double-checked by hydrogen gas manometry (HGM), Fourier transform infrared spectrometry (FT-IR), and secondary ion mass spectrometry (SIMS) to confirm consistency among different methods (Supplementary Fig. 1 and Supplementary Table 1).

As some glass inclusions and embayments were affected by devitrification, particularly in the pyroclastic deposits, the glass samples were examined using both optical microscopy and SEM to confirm that there was no crystallization. To avoid the effect of post-eruption hydration (Supplementary Fig. 2), analytical values within $30 \mu\text{m}$ of the glass surface were not used. To minimize the effect of rapid dehydration during ascent in the conduit, glasses occurring deeper than $\sim 100 \mu\text{m}$ from the surface of the host phenocryst were measured for the water content in the “plateau” part of embayments.

Diffusion model. We modeled the development of the water content profile in a $300\text{-}\mu\text{m}$ -long melt embayment filled with rhyolite melt, using a one-dimensional diffusion model. The modeled melt embayment connects to the melt outside on one side, and the other end is closed in the host crystal. The diffusion coefficient of water in the rhyolite melt is assumed as $1 \mu\text{m}^2 \text{ s}^{-1}$ at 800°C ⁴⁸. The temperature of the magma used in the model is based on the equilibrium temperature of magnetite-ilmenite pairs in the Osumi pumice fall deposit ($780\text{--}840^\circ\text{C}$)³³. The pressure dependence of the solubility of water is taken from published constraints³⁴.

For the modeling of magma-chamber decompression in the first step, the initial water content in the melt was assumed as $6.5 \text{ wt}\%$, based on the water content in the plateau part of the glass embayments of the Osumi pumice fall deposit (Fig. 2a and b). This water content corresponds to the saturated water content of rhyolite magma at 223 MPa ³⁴. We examined the profile of water contents in a melt embayment when the melt on the outside of an embayment dehydrates at various decompression rates ranging from $1 \times 10^2 \text{ Pa s}^{-1}$ to $1 \times 10^5 \text{ Pa s}^{-1}$ (Supplementary Figs. 3 and 4).

For the modeling of second-step decompression in the conduit, cases with initial water content of 6.5% , 6% , and 5% were modeled, depending on the degree of decompression dehydration in the magma reservoir. The profiles of water contents in a melt embayment were examined when the melt on the outside of an embayment dehydrates at various decompression rates ranging from $10 \times 10^3 \text{ Pa s}^{-1}$ to $500 \times 10^3 \text{ Pa s}^{-1}$ (Supplementary Fig. 5).

Deformation model. The elastic response to magma discharge was calculated using a 3D finite-element code, oregono_ve⁴⁹. The modeled rectangular parallelepiped domain had a thickness of 100 km and a horizontal dimension of $192 \times 192 \text{ km}$. The mechanical boundary condition corresponded to the traction on the top surface of zero in any direction, and normal displacement and tangential traction of zero for the rest of the boundary surfaces. The elastic properties, shear modulus, ($\mu = 10^{10} \text{ Pa}$), and Poisson’s ratio ($\nu = 0.25$) were constant in the model. A cylindrical magma chamber with a radius of r and a thickness of h was used for the calculation. The chamber was positioned at the center of Aira caldera, where the deflation source during the 1914 eruption and subsequent inflation source were

assumed to be located. The depths to the top and bottom of the magma chamber were assumed to be 6 and 9 km, respectively, based on the initial water content (5–6.5 wt%) in the embayment and inclusions of the Osumi pumice fall deposit, which corresponds to a pressure of approximately 140–250 MPa. The radius of the magma chamber (r) was assumed to be 7 km, based on the area of the caldera floor. The volume of the magma chamber was 462 km³, which corresponds to the total erupted volume of the AT eruption of ~400 km³. However, we ignored this original finite thickness of the chamber by applying a simple dislocation model for an instantaneous deflation at a depth of 7 km, for which the split-node method developed in a previous study⁵⁰ was adopted in the finite-element code used in this study⁴⁹. This approximation may be validated by the ratio of the half-thickness of the chamber to the depth ($\sim 1.5/7 = \sim 0.2$).

Data availability

The compositions and water contents of the glass inclusions and embayments have been deposited in “Figshare”. <https://doi.org/10.6084/m9.figshare.15146955>.

Received: 21 January 2021; Accepted: 8 September 2021;

Published online: 29 September 2021

References

- Robock, A. Volcanic eruptions and climate. *Rev. Geophys.* **38**, 191–219 (2000).
- Orsi, G., Di Vito, A.M. & Isaia, R. Volcanic hazard assessment at the restless Campi Flegrei caldera. *Bull. Volcanol.* **66**, 514–530 (2004).
- Self, S. & Blake, S. Consequences of explosive supereruptions. *Elements* **4**, 41–46 (2008).
- Self, S. Explosive super-eruptions and potential global impacts. In: *Volcanic Hazards, Risks and Disasters* (eds Shroder, J. F. & Papale, P.) 399–418. (Elsevier, 2015).
- Newhall, C., Self, S. & Robock, A. Anticipating future Volcanic Explosivity Index (VEI) 7 eruptions and their chilling impacts. *Geosphere* **14**, 572–603 (2018).
- Papale, P. & Marzocchi, W. Volcanic threats to global society. *Science* **363**, 1275–1276 (2019).
- Martí, J., Geyer, A. & Folch, A. A genetic classification of collapse calderas based on field studies and analogue and theoretical modelling. In *Studies in volcanology: The legacy of George Walker. Spec. Pub. IAVCEI*, 2 (eds Thordarson, T., Self, S., Larsen, S., Rowland, S. K. & Houskuldsson, A.) 249–266 (Geological Society of London, 2009).
- Druitt, T. H. & Sparks, R. S. J. On the formation of caldera during ignimbrite eruptions. *Nature* **310**, 679–681 (1984).
- Bacon, C. R. Eruptive history of Mount Mazama and Crater Lake caldera, Cascade Range, USA. *J. Volcanol. Geotherm. Res.* **18**, 57–115 (1983).
- Self, S., Rampino, M. R., Newton, M. S. & Wolff, J. A. Volcanological study of the great Tambora eruption of 1815. *Geology* **12**, 659–663 (1984).
- Rosi, M., Vezzoli, L., Castelmennano, A. & Grieco, G. Plinian pumice fall deposit of the Campanian Ignimbrite eruption (Phlegrean Fields, Italy). *J. Volcanol. Geotherm. Res.* **91**, 179–198 (1999).
- Kennedy, B.M., Mark Jellinek, A. & Stix, J. Coupled caldera subsidence and stirring inferred from analogue models. *Nat. Geosci.* **1**, 385–389 (2008).
- Williams, S.N. & Self, S. The October 1902 Plinian eruption of Santa Maria volcano, Guatemala. *J. Volcanol. Geotherm. Res.* **16**, 33–56 (1983).
- Lavallée, Y., de Silva, S. L., Salas, G. & Byrnes, J. M. Explosive volcanism (VEI 6) without caldera formation: insight from Huaynaputina volcano, southern Peru. *Bull. Volcanol.* **68**, 333–348 (2006).
- Martí, J., Folch, A., Neri, A. & Macedonio, G. Pressure evolution during explosive caldera-forming eruptions. *Earth Planet. Sci. Lett.* **175**, 275–287 (2000).
- Geshi, N., Ruch, J. & Acocella, V. Evaluating volumes for magma chambers and magma withdrawn for caldera collapse. *Earth Planet. Sci. Lett.* **396**, 107–115 (2014).
- Andrews, B. J. & Gardner, J. E. Effect of caldera collapse on magma decompression rate: an example from the 1800 ¹⁴C yr BP eruption of Ksudach volcano, Kamchatka, Russia. *J. Volcanol. Geotherm. Res.* **198**, 205–216 (2010).
- Aramaki, S. Formation of the Aira caldera, southern Kyushu, ~22,000 years ago. *J. Geophys. Res.* **89**, 8485–8501 (1984).
- Liu, Y., Anderson, A. T. & Wilson, C. J. N. Melt pockets in phenocrysts and decompression rates of silicic magmas before fragmentation. *J. Geophys. Res.* **112**, B06204 (2007).
- Lloyd, A. S. et al. NanoSIMS results from olivine-hosted melt embayments: magma ascent rate during explosive basaltic eruptions. *J. Volcanol. Geotherm. Res.* **283**, 1–18 (2014).
- Ferguson, D.J. et al. Magma decompression rates during explosive eruptions of Kilauea volcano, Hawaii, recorded by melt embayments. *Bull. Volcanol.* **78**, 71 (2016).
- Befus, K. S. & Manga, M. Supereruption quartz crystals and the hollow reentrants. *Geology* **47**, 1–5 (2019).
- Myers, M. L., Druitt, T. H., Schiavi, F., Gurioli, L. & Flaherty, T. Evolution of magma decompression and discharge during a Plinian event (Late Bronze-Age eruption, Santorini) from multiple eruption-intensity proxies. *Bull. Volcanol.* **83**, 18 (2021).
- Nagaoka, S. The late quaternary tephra layers from the caldera volcanoes in and around Kagoshima bay, southern Kyushu, Japan. *Geograph. Rep. Tokyo Metropolitan Univ.* **23**, 49–122 (1988).
- Matumoto, T. The four gigantic caldera volcanoes of Kyushu. *Japanese J. Geol. Geogr.* **19**, 1–57 (1943).
- Kobayashi, T., Hayakawa, Y. & Aramaki, S. Thickness and grain-size distribution of the Osumi pumice fall deposit from the Aira caldera. *Bull. Volc. Soc. Japan* **28**, 129–139 (1983).
- Geshi, N. & Miyabuchi, Y. Conduit enlargement during the precursory Plinian eruption of Aira Caldera, Japan. *Bull. Volcanol.* **78**, 63 (2016).
- Ueno, T. Features, source, and eruption volume of the Tsumaya pyroclastic flow deposit of the Aira caldera, southern Kyushu, Japan. *Bull. Volcanol. Soc. Japan* **61**, 533–544 (2016).
- Ueno, T. Feature and formation mechanism of lithic fragment concentration zone of the Ito pyroclastic flow deposit, Aira Caldera, Japan. *Proc. Inst. Nat. Sci. Nihon Univ.* **42**, 129–147 (2007).
- Carey, S. & Sigurdsson, H. The intensity of Plinian eruptions. *Bull. Volcanol.* **51**, 28–40 (1989).
- Kawai, S. & Miyake, Y. Grain-size and mineral compositions of Aira-Tn tephra, Japan – an example of the lateral variation of wide-spread tephra. *Jour. Geol. Soc. Japan* **105**, 597–608 (1999).
- Geshi, N., Yamada, I., Matsumoto, K., Nishihara, A. & Miyagi, I. Accumulation of rhyolite magma and triggers for a caldera-forming eruption of the Aira Caldera, Japan. *Bull. Volcanol.* **82**, 44 (2020).
- Yasuda, A., Yoshimoto, M. & Fujii, T. The depth of a magma chamber associated with the Aira caldera formation. *Bull. Volc. Soc. Japan* **60**, 381–397 (2015).
- Liu, Y., Zhang, Y. & Behrens, H. Solubility of H₂O in rhyolitic melts at low pressure and a new empirical model for mixed H₂O-CO₂ solubility in rhyolitic melts. *J. Volcanol. Geotherm. Res.* **143**, 219–235 (2005).
- Toramaru, A. On the second nucleation of bubbles in magmas under sudden decompression. *Earth Planet. Sci. Lett.* **404**, 190–199 (2014).
- de Graffenried, R. L. & Shea, T. Using volatile element concentration profiles in crystal-hosted melt embayments to estimate magma decompression rate: assumptions and inherited errors. *Geochem. Geophys. Geosys.* **22**, E2021GC009672 (2021).
- Roche, O., Druitt, T. H. & Merle, O. Experimental study of caldera formation. *J. Geophys. Res.* **105**, 395–416 (2000).
- Hardy, S. Structural evolution of calderas: insights from two-dimensional discrete element simulations. *Geology* **36**, 927–930 (2008).
- Walker, G. P. L. Downsag calderas, ring faults, caldera size, and incremental caldera growth. *J. Geophys. Res.* **89**, 8407–8416 (1984).
- Acocella, V. Understanding caldera structure and development: an overview of analogue models compared to natural calderas. *Earth Sci. Rev.* **85**, 125–160 (2007).
- Cashman, K.V. & Giordano, G. Calderas and magma reservoirs. *J. Volcanol. Geotherm. Res.* **288**, 28–45 (2014).
- Todde, A., Cioni, R., Pistolesi, M., Geshi, N. & Bonadonna, C. The 1914 Taisho eruption of Sakurajima volcano: stratigraphy and dynamics of the largest explosive event in Japan during the twentieth century. *Bull. Volcanol.* **79**, 72 (2017).
- Yamashina, K. Volcanic Cloud Height of the 1914 Eruption at Sakurajima Volcano - discussions on documentary records and photographs. *Bull. Volcanol. Soc. Japan* **44**, 71–82 (1999).
- Iguchi, M. Magma movement from the deep to shallow Sakurajima Volcano as revealed by geophysical observations. *Bull. Volcanol. Soc. Japan* **58**, 1–18 (2013).
- Fukushima, D. & Kobayashi, T. Mechanism of generation and emplacement of the Tarumizu pyroclastic flow associated with Osumi Plinian eruption from Aira Caldera, Japan. *Bull. Volcanol. Soc. Japan* **45**, 225–240 (2000).
- Nash, W. P. Analysis of oxygen with the electron microprobe: applications to hydrated glass and minerals. *Am. Mineral.* **77**, 453–457 (1992).
- Devine, J. D., Gardner, J. E., Brack, H. P., Layne, G. D. & Rutherford, M. J. Comparison of microanalytical methods for estimating H₂O contents of silicic volcanic glasses. *Am. Mineral.* **80**, 319–328 (1995).
- Zang, Y. & Behrens, H. H₂O diffusion in rhyolitic melts and glasses. *Chem. Geol.* **169**, 243–262 (2000).
- Yamasaki, T. & Houseman, G. A. The signature of depth-dependent viscosity structure in post-seismic deformation. *Geophys. J. Int.* **190**, 769–784 (2012).

50. Melosh, H. J. & Raefsky, A. A simple and efficient method for introducing faults into finite element computations. *Bull. Seism. Soc. Am.* **71**, 1391–1400 (1981).
51. Geshi, N. Glass embayment compositions and water contents. <https://doi.org/10.6084/m9.figshare.15146955> (2021).

Acknowledgements

The authors would like to thank Ayumu Nishihara and Hideto Naruo for supporting the fieldwork. Part of the field work of this study was supported by the Nuclear Regulation Authority of the Japanese Government. The authors also thank the private land owners who permit the sampling.

Author contributions

N.G. planned the framework of the study. The sampling and microprobe analysis were done by N.G. Analysis of petrological characteristics and water diffusion was conducted by N.G. C.C. and I.M.. T.Y. developed the numerical model of ground deformation. The initial draft of the paper was written by N.G. and all three authors improved the paper.

Competing interests

The authors declare no competing interests.

Additional information

Supplementary information The online version contains supplementary material available at <https://doi.org/10.1038/s43247-021-00272-x>.

Correspondence and requests for materials should be addressed to Nobuo Geshi.

Peer review information *Communications Earth & Environment* thanks Ben Andrews and the other, anonymous, reviewer(s) for their contribution to the peer review of this work. Primary Handling Editors: Emma Liu, Joe Aslin. Peer reviewer reports are available.

Reprints and permission information is available at <http://www.nature.com/reprints>

Publisher's note Springer Nature remains neutral with regard to jurisdictional claims in published maps and institutional affiliations.



Open Access This article is licensed under a Creative Commons Attribution 4.0 International License, which permits use, sharing, adaptation, distribution and reproduction in any medium or format, as long as you give appropriate credit to the original author(s) and the source, provide a link to the Creative Commons license, and indicate if changes were made. The images or other third party material in this article are included in the article's Creative Commons license, unless indicated otherwise in a credit line to the material. If material is not included in the article's Creative Commons license and your intended use is not permitted by statutory regulation or exceeds the permitted use, you will need to obtain permission directly from the copyright holder. To view a copy of this license, visit <http://creativecommons.org/licenses/by/4.0/>.

© The Author(s) 2021